Biphysical coding metasurfaces for independent and continuous manipulations of electromagnetic and acoustic waves

Jin Song Ye,[1] Wen Kang Cao,[1,*] Kai Ping Nie,[1] Sheng He,[1] Kun Hong Li,[1] Qiao Huang,[1] Li Ting Wu,[2,†] and Jie Hu[1,‡]
[1]*School of Mechanical Engineering, Guizhou University, Guiyang 550025, China*
[2]*School of Communication and Artificial Intelligence, School of Integrated Circuits, Nanjing Institute of Technology, Nanjing 211167, China*

(Received 17 April 2025; accepted 10 July 2025; published 19 August 2025)

It still remains a significant challenge using the current technology to fabricate devices with customized functions for both electromagnetic (EM) and acoustic waves since the demand of biphysical manipulation, which means that the same device can be used to control EM and acoustic waves simultaneously, difficult is to satisfy in nature. However, the emergence of metasurfaces provides a new way to synchronously control the propagation for both waves. Unfortunately, the independent and continuous wavefront manipulation of multiple physical fields, including acoustic and EM waves, still requires overcoming significant challenges. In this study, we propose and demonstrate EM-acoustic biphysical coding metasurfaces (BCM) which are capable of independently engineering propagation behaviours for both waves. In addition, continuous phase tunability across each domain can be attained. Eight kinds of unit cells with different geometrical parameters which consist of dual-layers are employed to serve as 2-bit reflection-type meta-atoms, thus offering opportunities for almost arbitrary wavefront manipulation of EM and acoustic waves as desired. The simulation results demonstrate that the proposed BCM can perform different functionalities for dual waves, such as multiple-beam generation, focusing, and vortex beam generation, which can be flexibly switched by tuning coding sequences of unit cells. The research results can help to enrich functions of metasurfaces, expand their application scope, and pave the way for the development of biphysical multifunctional devices and applications in the future.

DOI: 10.1103/5b62-yd88

I. INTRODUCTION

Over the past decades, metasurfaces, as an artificial structured material, have attracted great attention and are widely used in various fields due to their ability to flexibly manipulate electromagnetic (EM) waves, acoustic waves, and elastic waves [1–3]. Therefore, many novel phenomena and unique functions have been demonstrated, such as negative refraction [4,5], abnormal beam steering [6], and cloak [7,8]. Moreover, it is hard to find natural materials to meet these demands of wave manipulations [9,10].

Furthermore, it has been a long dream to control EM and acoustic waves using the same device in a desired fashion. Recently, due to the unique characteristic of metasurfaces, some scholars have proposed biphysical manipulation, which means that the same metasurface can be used to control EM and acoustic waves simultaneously. In 2016, a carpet cloak based on metasurfaces was proposed which can synchronously control the local reflection phase of EM, acoustic, and water waves [11]. Whereafter, dual-physical metasurfaces which consist of membrane structures coated with indium tin oxide films are demonstrated to achieve excellent acoustic insulation and EM absorption/diffusion at the same time [12,13]. Subsequently, a 3-bit encoded metasurface capable of simultaneously manipulating acoustic and EM waves was proposed to realize various functionalities, such as scattering diffusion and beam scanning [14]. In recent years, researchers have proposed an EM-acoustic multiphysics field-compatible metasurface, which seamlessly integrates a microperforated plate structure with an EM metasurface [15]. This metasurface can achieve EM backward scattering reduction, digital infrared camouflage, and sound absorptivity meanwhile. The above research mainly focused on the EM-airborne acoustic biphysical metasurfaces. However, with the rapid development of biphysical metasurfaces, scholars started to explore the control of EM-underwater acoustic waves simultaneously. For example, an artificial ultrathin biphysical metamaterial for microwave and underwater acoustic absorption was designed, which was realized by the compatible integration of thin flexible copper patches and ultrathin polydimethylsiloxane with multisized air bubbles [16]. Although these research can achieve synchronous control of acoustic waves and EM waves, once the behaviors of acoustic waves change then the behaviors of EM waves must change accordingly and vice versa. Hence, this research did not have the ability to independently control both physical waves and functions that such metasurfaces can achieve in a limited way and may not be able to cope with some complex situations. To address these

*Contact author: wkcao@gzu.edu.cn
†Contact author: njltwu@hotmail.com
‡Contact author: jiehu@gzu.edu.cn

Published by the American Physical Society under the terms of the Creative Commons Attribution 4.0 International license. Further distribution of this work must maintain attribution to the author(s) and the published article's title, journal citation, and DOI.

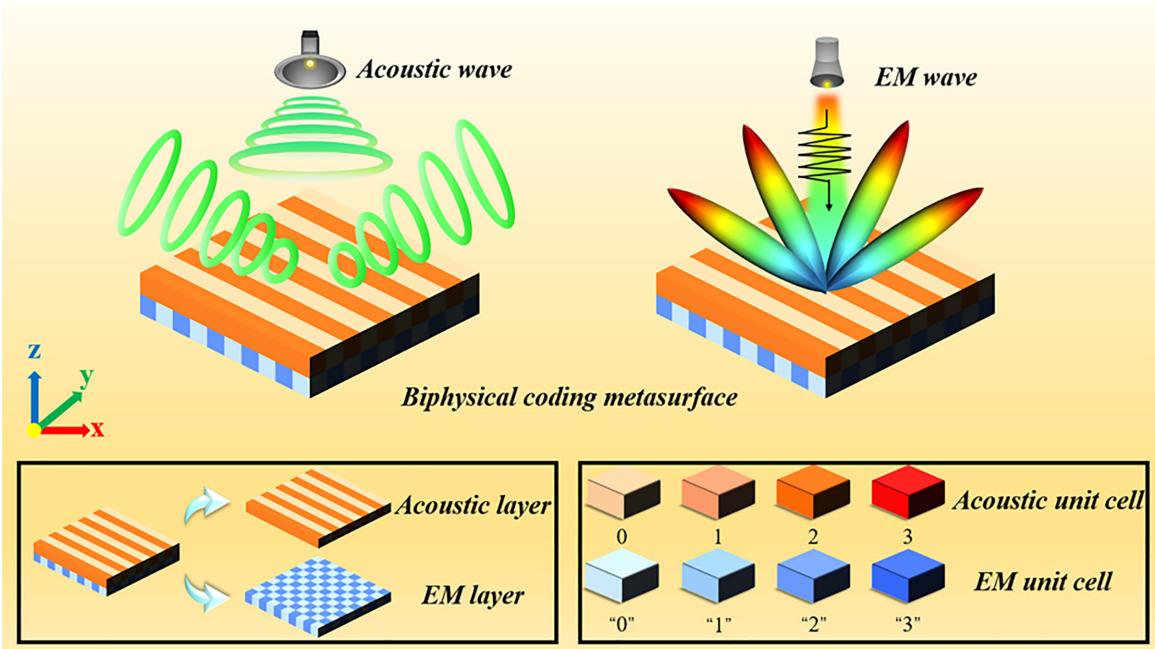


FIG. 1. The principal diagram of the proposed EM-acoustic BCM under the plane acoustic/EM incident waves along $-z$ direction. The proposed BCM with a dual-layer structure are composed of eight types of unit cells serving as 2-bit coding elements in biphysical fields.

drawbacks, scholars have conducted research on the independent control of EM and acoustic waves by metasurfaces and the behaviors of EM/acoustic waves can be adjusted without being disturbed by another wave. In 2019, Zhang achieved the independent control of acoustic-EM waves by changing the materials and geometries of meta-atoms to generate specific phase responses for both waves [17]. Later, a dual-physics metasurface for simultaneous manipulations of acoustic and EM waves emerged. In this work, this power-flow–conformal metasurfaces performed specified operations on both EM and acoustic waves at the same time [18]. Nevertheless, it should be pointed out that the phases of these proposed metasurfaces were barely continuously adjusted and the approximate 360° phase coverage cannot be realized. Hence, the prospect of their application and functions are still limited. Therefore, the proposed BCM in the article will realize not only the independent manipulation of EM and acoustic waves, but also the continuous phase tunability across each domain. Thus, the functions and application of the BCM prospects are more extensive.

Additionally, note that there is much research based on transformation optics/acoustics to realize biphysical cloaks [19–21]. In addition, conventional metasurfaces are usually characterized by huge quantities of meta-atoms with different geometrical shapes, bringing with it significant drawbacks, such as sophisticated design. To address this problem, recently, digital coding metasurfaces have emerged, which was composed of finite types of elements, as can be encoded by binary digits [22–24]. For example, the n-bit metasurface has 2^n basic elements with equal reflection amplitudes and a phase interval of $2\pi/2^n$. It was demonstrated that coding metasurfaces played a crucial role in wave regulation and realized various complicated functions, including scattering reduction [14], focusing [25], and holograms [26] at EM and acoustic regimes.

In this paper, the EM-acoustic biphysical coding metasurfaces (BCM) are proposed to control reflected phases of EM and acoustic waves independently and continuously. The proposed BCM consists of eight types of unit cells as meta-atoms, which have nearly unity reflection amplitudes and a phase interval of 90° suitable for 2-bit coding elements in both EM and acoustic responses, making it possible to obtain the aim of almost arbitrary wavefront manipulation of dual-physical fields. It is shown that EM/acoustic wavefronts of BCM can be modified independently by simply varying the coding sequences of unit cells. Furthermore, using the proposed unit cells, several 2-bit coding states are created for dual-physical fields, from which various functions, such as multiple-beam generation, focusing, and vortex beam generation, can be built and are confirmed by simulations.

II. THEORY AND DESIGN

Figure 1 shows the conceptual diagram of the proposed EM-acoustic BCM, which illustrates different acoustic scattering characteristics (left inset) and EM ones (right inset) under normal illustration from two kinds of waves with operating frequency 10 467 Hz for acoustic waves and 10 GHz for EM waves. Here, the BCM are the dual-layer structure, which consists of an upper layer (acoustic layer) and a bottom layer (EM layer). Eight types of unit cells are divided into two groups for basic elements as acoustic unit cells or EM ones, respectively. The reflection phase of EM and acoustic waves can be independently and continuously controlled by adjusting the parameters of these unit cells, which will be confirmed in the following. For simplicity, when the reflected phase of acoustic waves changes from −180° to 180°, the 2-bit phases are encoded as 0, 1, 2, and 3, corresponding to the four coding elements with a phase interval of 90°, respectively; similarly, the 2-bit EM reflected phases are named as

TABLE I. EM and acoustic parameters of the used materials.

Name	Density ρ (kg/m^3)	Speed of sound c (m/s)	Permittivity
Air	1.29	343.0	1.0
FR-4	1800	410.3	4.3(1+i0.025)
Copper	8930	4720	
Epoxy resin	1200	2692	3.3; tan$\delta \leqslant 0.004$

"0," "1," "2," and "3." In this work, the proposed EM-acoustic BCM are encoded with different coding sequences of unit cells and independent wavefront manipulations for both EM and acoustic waves can be achieved.

To achieve the desired wavefront manipulation of biphysical fields, the acoustic layer of BCM barely affects the transmission of EM waves. Moreover, the EM layer can be used to achieve total reflection of acoustic waves. Hereafter, the acoustic layer and EM layer can be utilized to adjust the wavefront of dual waves, respectively. Specifically, the reflectance and transmittance characteristics between the medium (air) and BCM are determined by intrinsic impedances of them. For EM fields, the effective impedance of BCM can be expressed as

$$Z_{\mathrm{EM}} = \sqrt{\mu/\varepsilon}, \tag{1}$$

where μ and ε are the effective permeability and permittivity, respectively. The reflectivity of EM waves at the interface between air and BCM can be expressed by the following equation:

$$\Gamma_{\mathrm{EM}} = \frac{Z_{\mathrm{EM}} - Z_0}{Z_{\mathrm{EM}} + Z_0}, \tag{2}$$

where Z_0 is the EM impedance of air. Similarly, for the acoustic field, the effective acoustic impedance of the BCM can be calculated according to the following equation:

$$Z_{\mathrm{Sound}} = \rho c. \tag{3}$$

Among them, c and ρ represent the effective sound velocity and density of the BCM. In analogy with the reflectivity of EM waves, the reflectivity of acoustic waves at the interface between the BCM and air (where Z_{Air} is the acoustic impedance of air) is obtained:

$$\Gamma_{\mathrm{Sound}} = \frac{Z_{\mathrm{Sound}} - Z_{\mathrm{Air}}}{Z_{\mathrm{Sound}} + Z_{\mathrm{Air}}}. \tag{4}$$

According to Eqs. (2) and (4), the EM impedance of the acoustic layer should approximate consistently with that of air to achieve the total transmission of EM waves; the acoustic impedance of the EM layer should be much larger than that of air to obtain the total reflection of acoustic waves. Table I gives the density, sound velocity, and permittivity of air, FR-4 [12], copper, and epoxy resin. The copper has high electrical conductivity (5.96×10^7 S/m) and the corresponding permittivity approaches infinity near low frequencies [17]. Obviously, it can be found that the acoustic impedances of F4b and epoxy resin are much higher than that of air. Hence, the FR-4 and copper are chosen to consist of the material of the EM layer. Moreover, to maintain an approximate total transmission of EM waves for the acoustic layer of BCM, it is necessary to ensure that the selected material of the acoustic layer has a relative low permittivity to meet the EM impedance matching between BCM and air. Therefore, the epoxy resin is chosen as the material of the acoustic layer.

Next, to achieve the proposed EM-acoustic BCM, a typical structure of unit cell is proposed using the materials in Table I, as shown in Figs. 2(a) and 2(b). Initially, the proposed unit cell with the period p and height h is composed of two sections (acoustic layer and EM layer), which is consistent with the proposed EM-acoustic BCM in Fig. 1. Specifically, the acoustic layer is a square cavity structure without the bottom board. The neck width of the cavity w_1 is a tunable parameter for controlling the acoustic reflected phase shift of the unit cell and the thickness of the wall t_c is fixed [Fig. 2(c)]. In addition, the EM layer consists of three layers with the total thickness t. A square copper patch with the side length w_2 and thickness t_2 is etched into a dielectric substrate (FR-4) with thickness t_1 and a copper ground with thickness t_3 is located at the bottom of the dielectric substrate to block the backward EM scattering. Here, the varying side length w_2 can be used to require the desired EM reflected phases. The fixed geometrical parameters of the proposed unit cell are $p = 15$ mm, $h = 5.035$ mm, $t_c = 1$ mm, $t_1 = 1$ mm, $t_2 = t_3 = 0.035$ mm.

To study the reflection characteristics of the proposed unit cell, commercial numerical solvers comsol Multiphysics 6.1 and CST Studio Suite 2023 are employed to analyze and calculate the reflection amplitude and phase of the unit cells in acoustic and EM simulations, respectively, where the plane wave is vertically incident on the unit cell and periodic boundaries are applied around it.

For the simulation of acoustic wavefront manipulation, because the acoustic impedance of the unit cell is far greater than that of the air, the materials of the unit cell can be regarded as acoustically rigid and the thermoviscous losses are negligible. Moreover, because the thickness of copper patches and copper ground of EM layers (0.035 mm) is much less than the acoustic wavelength (30 mm) in air, the introduction of that is a negligible influence on the acoustic response of metasurfaces [12]. Hence, for calculating acoustic near/far field distributions in the following, copper patches and the ground are ignored to reduce computation. However, calculating the acoustic reflection spectra of unit cells, these are considered for ensuring the accuracy. In addition, the amplitude of the incident acoustic wave is set to 1 Pa and the reflected amplitude and phase can be extracted using a standard transfer matrix method in matlab from simulated reflection spectra. Specifically, to validate that the thermoviscous losses are negligible, simulated comparison results for the reflected amplitude and phase of acoustic waves with and without considering thermoviscous losses are added in the main text (Fig. 3). Obviously, the reflection amplitude is slightly impacted when thermoviscous losses are introduced with $w_2 = 1.5$ mm, while the reflection phase is hardly altered in Figs. 3(a) and 3(b). Hence, the thermoviscous losses are not considered in the following simulations for acoustic fields due to the negligible thermoviscous losses.

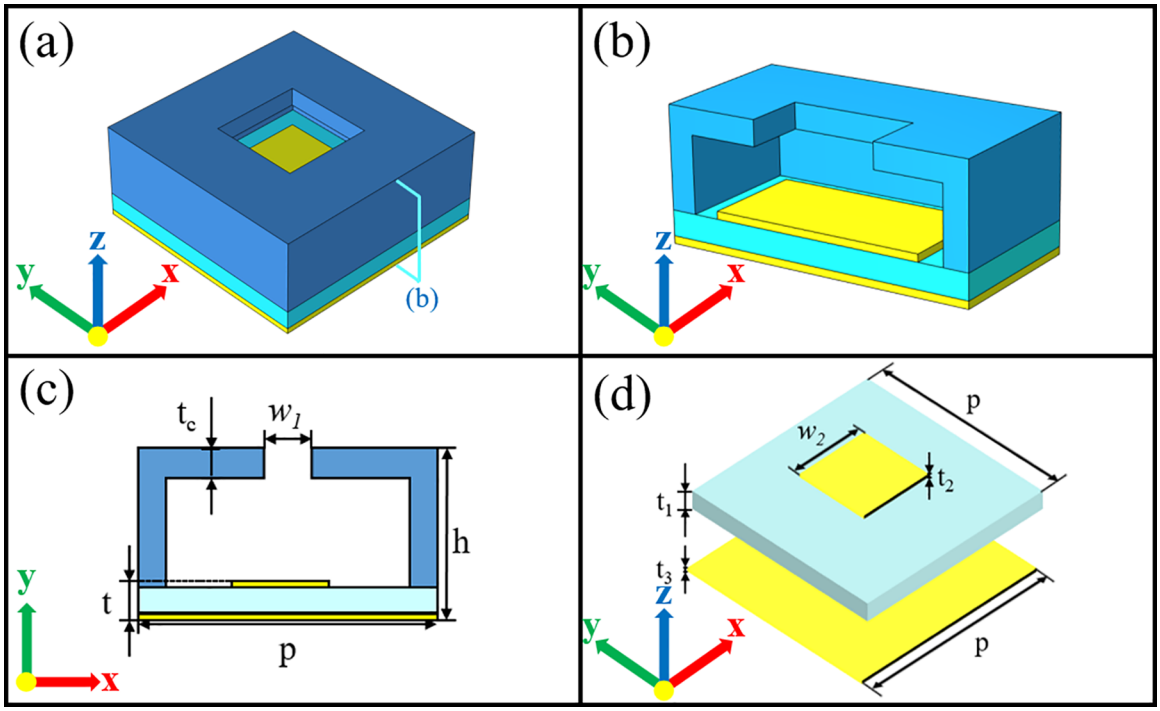


FIG. 2. (a) The basic structure of the proposed unit cell with the period p and height h. (b) Cross-section view of the unit cell. (c), (d) The detailed geometric parameters of the unit cell.

Next, the simulated acoustic and EM reflection spectra for the proposed unit cells are demonstrated in Fig. 4. In detail, Figs. 4(a) and 4(b) respectively show the reflection amplitudes of acoustic/EM waves as function of w_1 or w_2. It can be found that the minimum reflection amplitudes for dual waves are both 0.99. Figure 4(c) shows the acoustic reflection phase of the proposed unit cell. It is easy to observe that an approximate 310° span of the reflection phase shift can be observed, as w_1 increases from 0.1 mm to 12 mm, while the varying w_2 has no effect on phases. Hence, four kinds of acoustic layers for the proposed unit cells with the phase interval 90° are selected as 2-bit coding meta-atoms for the manipulation of acoustic wavefront and the corresponding geometrical parameters of w_1 are identified by the pentagrams in Fig. 4(c). In addition, in the EM regime, another four kinds of unit cells are also highly reflective. Meanwhile, the four phase traces nearly coincide and a phase shift of nearly 300° is displayed. It is implied that the EM layers with different w_1, identified by the pentagrams in Fig. 4(d), are selected as the EM layers of the proposed unit cells with 2-bit coding states. However, it can be found that the varying w_1 has barely am effect on the EM reflected phases. According to the above simulation results, it can be seen that the reflected phase of the acoustic waves is mainly affected by the size of the neck width of the cavity w_1, while the reflected phase of the EM waves is mainly affected by the size of the square copper patch; therefore, w_1 and w_2

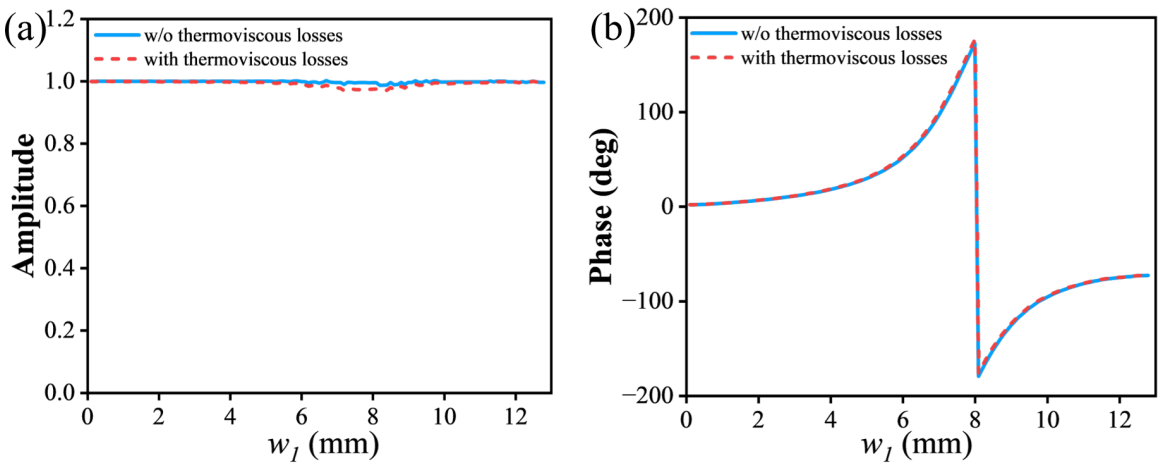


FIG. 3. The influence of thermoviscous losses on reflected (a) amplitude and (b) phase of acoustic waves with $w_2 = 1.5$ mm.

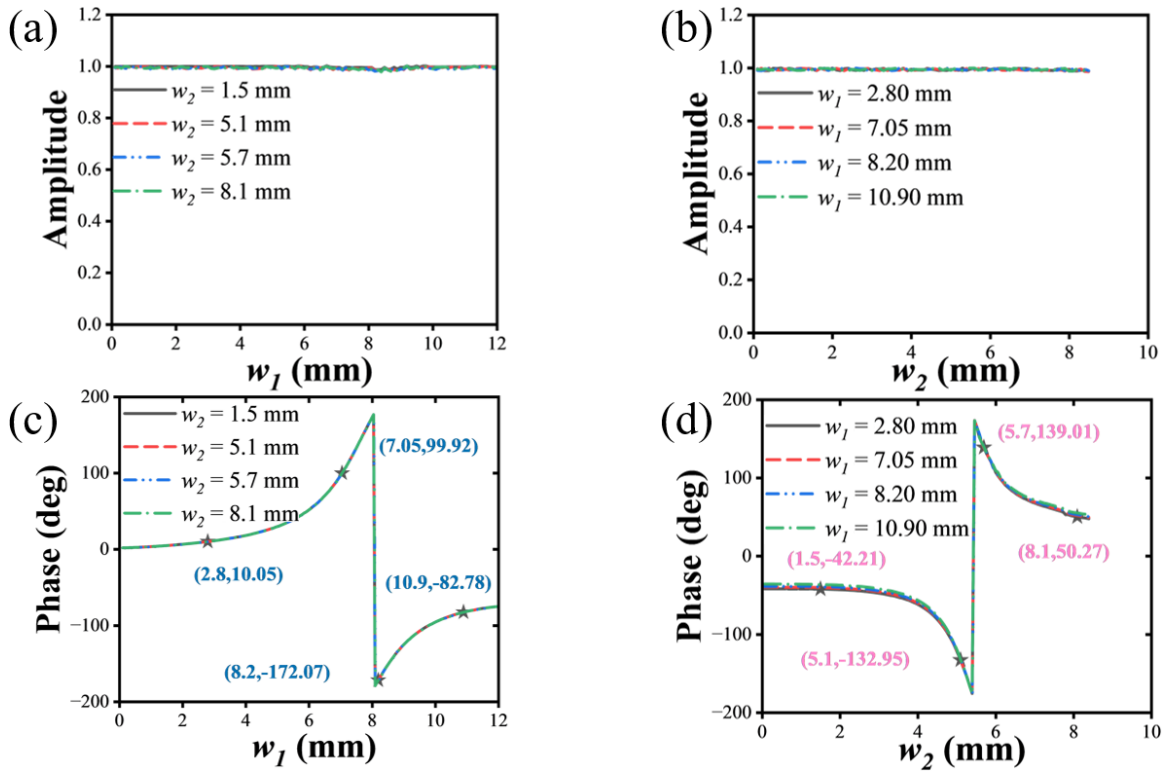


FIG. 4. The simulated acoustic and EM reflection spectra for the proposed unit cells as a function of w_1 and w_2. (a) The simulated acoustic reflection amplitude. (b) The simulated EM reflection amplitude. (c) The simulated acoustic reflection phase. (d) The simulated EM reflection phase. The pentagrams in (c) and (d), represent the required phase for acoustic and EM fields, respectively.

can be utilized to independently and continuously control the phase of acoustic or EM waves, respectively. Furthermore, through the combination for the 2-bit coding states of acoustic and EM layers, the corresponding unit cells can be used to encode the EM-acoustic BCM which can be used for the independent control of dual fields by synthesizing phases of reflected waves with proper coding sequences of unit cells. The specific structures of 2-bit coding states for acoustic and EM layers are shown in Fig. 5.

III. WAVEFRONT MANIPULATION VIA THE PROPOSED EM-ACOUSTIC BCM

The 2-bit coding sequences have strong abilities to generate multiple beams, focus, and vortex beams that carry the orbital angular momentum. Here, by the proposed unit cells, the independent beams control of biphysical fields is introduced. Under the illustration of EM/acoustic waves, the scattering pattern of the BCM can be demonstrated as [27,28]

$$f(\theta,\varphi) = f_e(\theta,\varphi)\sum_{m=1}^{M}\sum_{n=1}^{N}\exp\{-i\{\varphi(m,n) + k_0 D\sin\theta[(m-1/2)\cos\varphi + (n-1/2)\sin\varphi]\}\}, \tag{5}$$

where m and n represent the row and column numbers in the BCM. θ, φ, and k_0 are the elevation, azimuth angles, and the wave number of air, respectively. $f_e(\theta,\varphi)$ is the pattern function of a unit cell and $\varphi(m,n)$ is the reflection phase of the lattice (m,n). D is the period of coding element. According to Eq. (5), far field scattering patterns of the proposed BCM can be changed by adjusting coding sequences of coding elements. Scattering beams pointing to different directions can be obtained through the modulation of coding sequences for unit cells with different coding states. Specifically, as shown in Fig. 6(a), several dual-layers compose three different coding sequences C1, C2, and C3. Here, the coding sequence of acoustic layer is defined as M1 and that of the EM one is defined as M2. The EM-acoustic BCM comprise 2×2 supercells and each supercell, representing a coding element 0 or 2, consists of 2×2 identical unit cells. In the upper row of Fig. 6(a), the coding sequence C1 consist of both M1 and M2 which are 02020202 along the x and y directions, respectively. The corresponding three-dimensional (3D) EM and acoustic far field scattering patterns of BCM are demonstrated in Figs. 6(b) and 6(h). Clearly, two pairs of scattering beams symmetrically distributed with respect to the normal direction emerge, when EM and acoustic plane waves are incident along the $-z$ direction. According to the generalized Snell's law, the reflection angle θ_r can be calculated as [17]

$$\theta_r = \arcsin\frac{\lambda}{L}, \tag{6}$$

where λ are the wavelength and $L = 60$ mm stands for the period length with gradient phase. As illustrated by Eq. (6), the theoretical reflection angles of both EM and acoustic waves are 30°, which are consistent with the simulated results (29.7°) of two-dimensional (2D) EM and acoustic far field

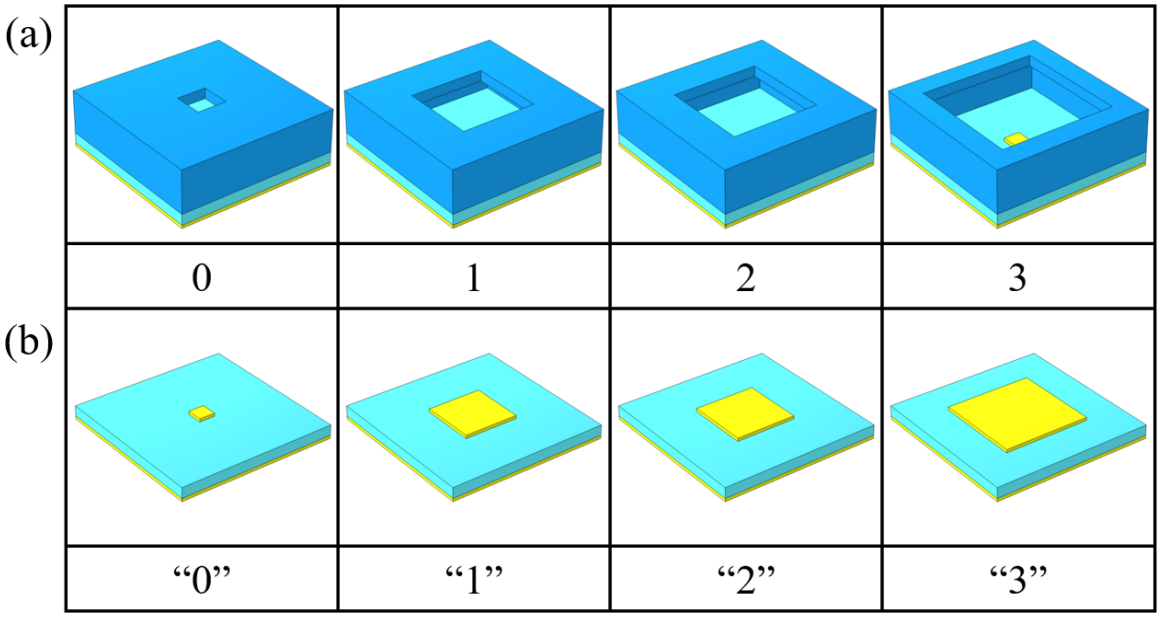


FIG. 5. (a) Structures of 2-bit acoustic coding states and (b) EM ones without acoustic layers.

scattering patterns [Figs. 6(e) and 6(k)] in the *yoz* and *xoz* planes, respectively.

Next, the coding sequence M1 is altered to a checkerboard-like coding sequence, while keeping M2 unchanged, as illustrated in the middle row of Fig. 6(a). It is reasonably predicted that the EM far field scattering pattern remains unchanged approximately, which is confirmed by the simulated EM far field scattering pattern in Figs. 6(c) and 6(f). However, the 3D acoustic far field scattering pattern demonstrates that four-scattering beams with the same maximum sound pressure level (SPL) are obtained [Fig. 6(i)] due to the equal amplitudes of phase gradients in both the $\pm x$ and $\pm y$ directions, which is well validated by the simulated 2D result in Fig. 5. Similarly, as illustrated in the bottom row of Fig. 6(a), the coding sequence C3 consists of two checkerboard-like coding sequences M1 and M2. Hence, two sets of four-scattering beams

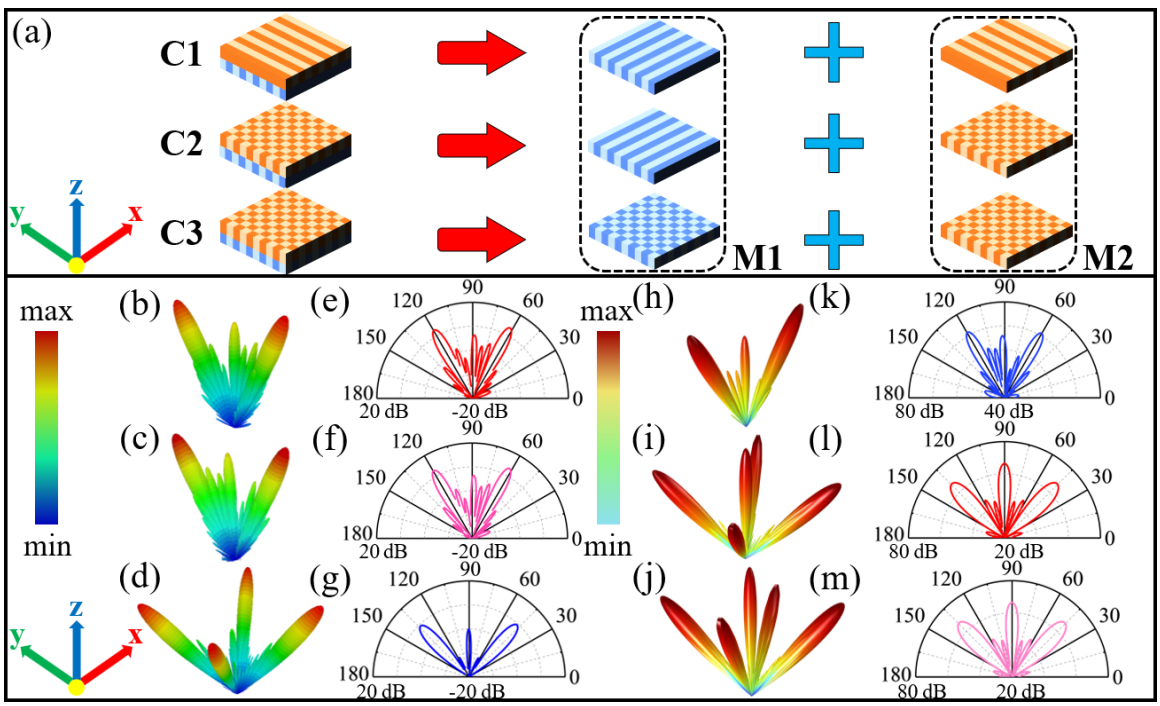


FIG. 6. Schematic of the patterned EM-acoustic BCM and the corresponding EM scattering patterns and acoustic ones under normal incidence. (a)–(c) The coding sequence C1, C2, and C3 which consist of dual-layer structure with coding sequences M1 and M2. (b)–(d) The 3D EM far field scattering patterns and (e)–(g) the 2D ones corresponding to the BCM in (a). (h)–(j) The 3D acoustic far field scattering patterns and (k)–(m) the corresponding 2D ones corresponding to the BCM in (a).

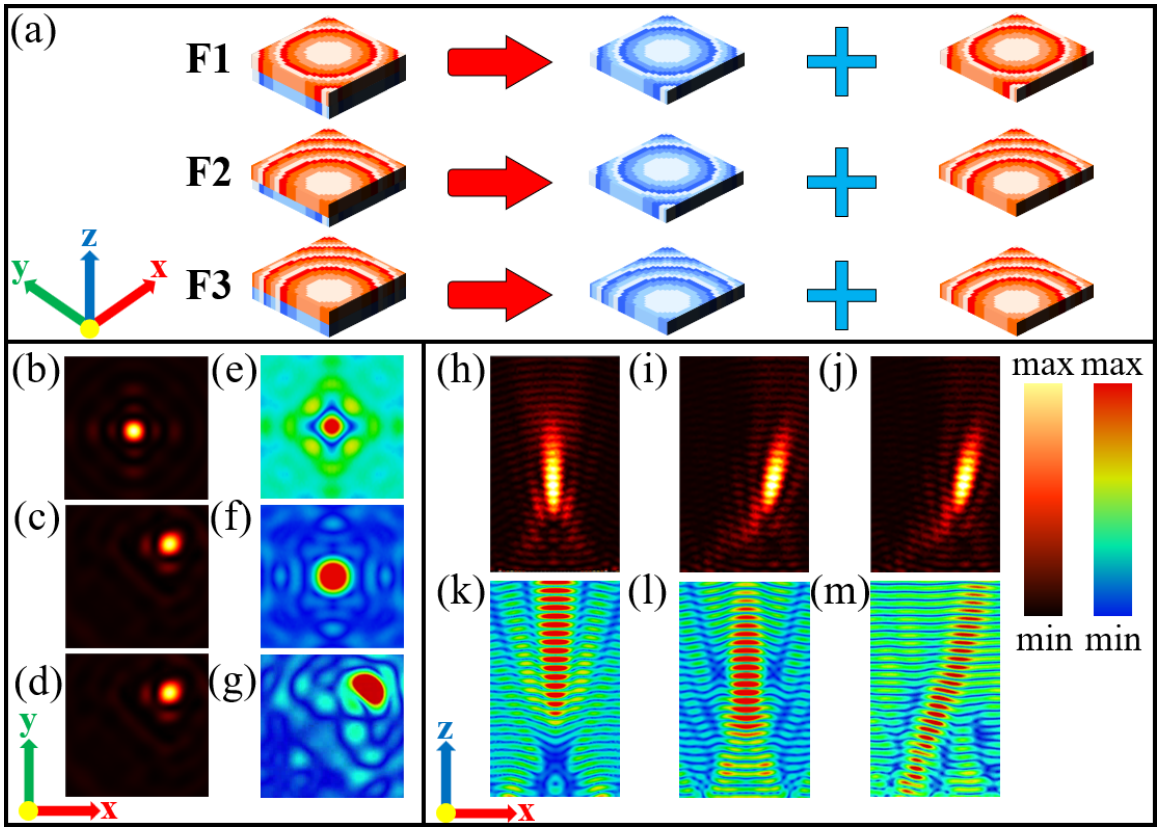


FIG. 7. Schematic of the proposed EM-acoustic biphysical focus metalenses and the corresponding reflected acoustic/EM intensity distributions. (a) Three sets of coding sequences are F1, F2, and F3, respectively. (b)–(d) and (e)–(g) are the acoustic/EM intensity distribution in the *xoy* plane. (h)–(j) and (k)–(m) are the corresponding ones in the *xoz* plane.

for EM and acoustic fields are achieved in Figs. 6(d) and 6(j), respectively. Such a property is validated by the 2D simulation results in Figs. 6(g) and 6(m). The simulation results in Fig. 6 prove that the proposed BCM can be utilized to independently engineer the wavefronts of EM/acoustic reflected waves via flexibly arrangement of coding sequences for BCM to realize the generation of multibeams.

As a practical application, the focus metalens operating at EM or acoustic fields has shown great practical application values in engineering procedures [29,30]. However, a dual-function focus device, operating at biphysical fields, can have greater application values in nondestructive testing [31] and biomedical diagnosis [32]. Next, we will further demonstrate a biphysical focus metalens via the proposed BCM. As shown in Fig. 7(a), three biphysical focus metalenses encoded by coding sequences F1, F2, and F3 are also composed of two layers. Here, the biphysical focus metalenses consists of different arrays with 2-bit EM/acoustic meta-atoms, which are marked by different color using coding elements in Fig. 4. When the EM/ acoustic waves are incident perpendicularly along the $-z$ direction, the phase distribution of the biphysical focus metalenses can be expressed as [33]

$$\phi(x, y) = k[\sqrt{{z_f}^2 + (x - x_f)^2 + (y - y_f)^2} - z_f], \quad (7)$$

where (x_f, y_f, z_f) is the focal coordinates and k is the wave number. It is obvious that the proposed metalens can be used meanwhile to focus the energy of EM and acoustic waves at most any position in the upper space of the BCM by arranging the unit cells with reasonable coding sequences based on Eq. (7).

Here, to demonstrate that the focal spot locations of EM/acoustic fields can be adjusted independently via the proposed metalens, in the upper row of Fig. 7(a), this metalens can be used to focus EM and acoustic waves with the same focal spot location (120, 120, 30 mm). Figures 7(b) and 7(h) show the reflected acoustic intensity distributions of the proposed biphysical focus metalens in the *xoy* and *xoz* planes, respectively. It is obvious that the energy of the reflected waves is focused on a limited area on the central axis. The near field distributions of EM waves for the proposed metalens in Figs. 7(e) and 7(k) also illustrate the similar phenomenon for focusing. Furthermore, by changing the coding sequence of the upper layers for the proposed metalens, while the bottom layer of it is unchanged, the coding sequence F2 is obtained in the middle row of Fig. 7(a). Figures 7(c) and 7(i) show an obvious offset-axis acoustic focus with focal spot location (180, 180, 30 mm). However, due to the same coding sequence of the bottom layer with F1, the EM focus characteristics of this metalens in Figs. 7(f) and 7(l) are almost consistent with that in the Figs. 7(e) and 7(k). In addition, the double offset-axis fucus for biphysical field can be achieved using the coding sequences F3 in the bottom row of Fig. 7(a), which is confirmed by the simulated acoustic/EM intensities distributions in Figs. 7(d) and 7(j) as well as Figs. 7(g) and 7(m).

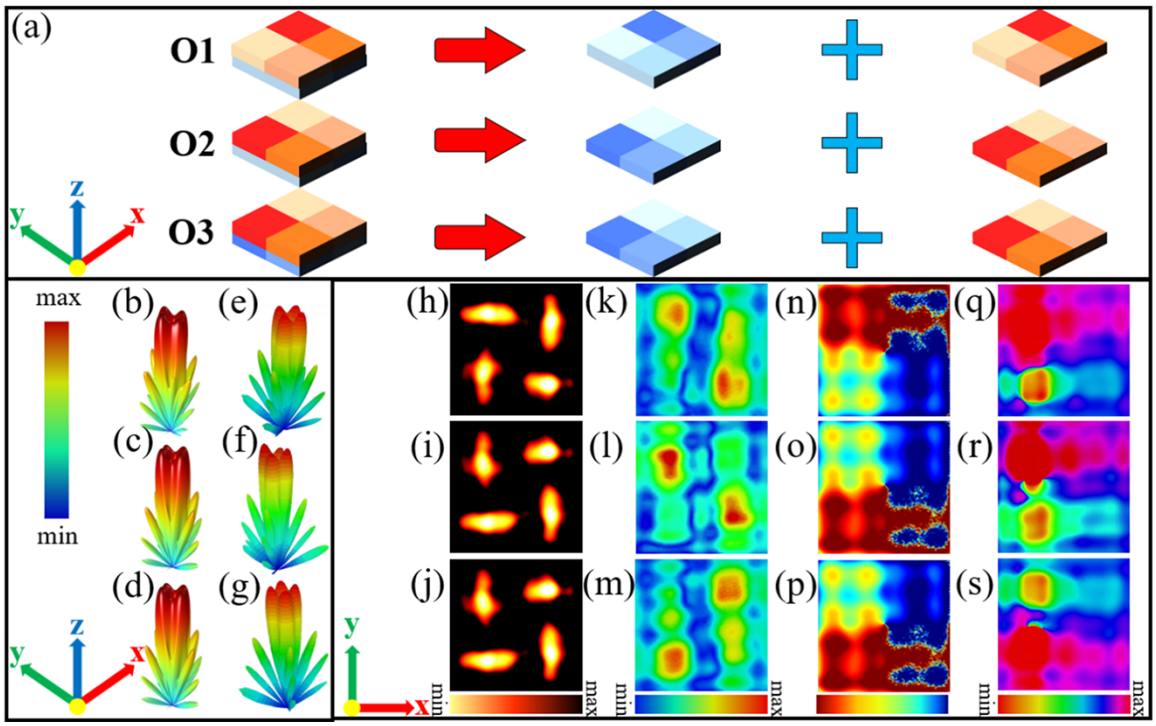


FIG. 8. Schematic of the proposed EM-acoustic biphysical vortex beam generation and the corresponding reflected acoustic/EM intensity distribution. (a) Three sets of coding sequences are O1, O2, and O3, respectively. (b)–(d) and (e)–(g) are the acoustic/EM 3D far field scattering patterns corresponding to the coding sequences in (a). (h)–(j) The corresponding acoustic near-field amplitude and (n)–(p) phase distributions. (k)–(m) The corresponding EM near-field amplitude and (q)–(s) phase distributions.

At the moment, both the EM/acoustic focal spot locations are (180, 180, 30 mm).

To further demonstrate more complex and flexible wavefront manipulation of the proposed BCM, due to 2-bit digital codes, the biphysical vortex beams carrying the orbital angular momentum (OAM) mode with different topological charges l can be achieved. The OAM beams have attracted much attention because they have great application values in communication [34] and particle manipulation [35]. However, the OAM beams with independent EM/acoustic wavefront control and mode orthogonality will have greater potential application, such as multifunctional cooperative communication and particle manipulation with a high degree of freedom. Mathematically, the OAM beams have a typical azimuthal phase dependence $\exp(il\varphi)$ and the phase distribution can be expressed as [14]

$$\phi(x, y) = l\varphi = l\arctan(\gamma/x), \tag{8}$$

where φ refers to the azimuth angle. In the following, three sets EM/acoustic BCM will be demonstrated to achieve OAM beams with variable topological charges in dual fields. In Fig. 8(a), the proposed BCM are encoded with coding sequences O1, O2, and O3, respectively. As illustrated in Figs. 8(h) and 8(n), the reflected acoustic near field amplitude and phase distributions display a hollow occurs in the center of OAM beam, which corresponds to the character of the vortex beam. Such a property is again validated by the 3D far field scattering pattern in Fig. 8(b). The corresponding EM OAM beams demonstrate similar characteristics in Figs. 8(e), 8(k), and 8(q). Because of the independent wavefront manipulation of the proposed BCM, the topological charges of EM/acoustic OAM beams can be flexibly changed. In the middle row of Fig. 8(a). the upper layer of the BCM is changed and the bottom layer remains unchanged. It is clear that the acoustic far/near field distributions are altered and an OAM with the topological charge of -1 order is obtained in Figs. 8(c), 8(i), and 8(o). However, the topological charge of the EM OAM beam is invariable [Figs. 8(f), 8(l), and 8(r)] by the BCM encoding with coding sequence O2. In addition, the biphysical OAM beams with both topological charges of -1 order can be achieved by encoding the BCM with coding sequence O3 [the bottom row in Fig. 8(a)]. Here, the acoustic far/near field distributions in Figs. 8(d), 8(j), and 8(p) coincide well with that in Figs. 8(c), 8(i), and 8(o) and the EM OAM beam demonstrates that the EM amplitude and phase distributions have an obvious character of the vortex beam with topological charge of -1 order, as illustrated in Figs. 8(g), 8(m), and 8(s). As in previous examples, the EM/acoustic wavefront of the proposed BCM can be independently engineered and the EM/acoustic reflected phase can be continuously adjusted, making it flexible to achieve complex biphysical wave-control devices.

IV. CONCLUSION

In summary, we propose and demonstrate the EM-acoustic BCM which can independently and continuously control the reflected phase of dual fields. A dual-layer unit cell is utilized to generate the desired phase responses for EM or acoustic waves via adjusting the size of the copper patch or cavity

of unit cells, which can act as the 2-bit coding elements in each wave. The EM/acoustic wavefront of the BCM can be deliberately changed by adjusting the coding sequences of the proposed unit cells. In addition, benefiting by the design of dual layers, functions for the manipulation of EM and acoustic waves can be independently altered. As examples, biphysical multiple-beam generation, focus metalenses, and vortex beam generation are demonstrated by numerical results in both the EM and acoustic domains. Regarding the application scenarios, the proposed BCM can have application values in many fields. In autonomous driving systems, both automotive ultrasonic radars and millimeter-wave radars are indispensable sensors and each sensor can offer a unique function and advantages. However, the proposed BCM can achieve integration and miniaturization of devices by combining both systems because of the independent manipulations of EM and acoustic waves as well as continuous phase tunability across each domain. In addition, our BCM can be used to achieve the EM and acoustic invisibility within a single device, significantly reducing the probability of the military platforms being exposed. Finally, the proposed BCM can facilitate the development of EM-acoustic biphysical communication devices by fully leveraging the advantages of both waves. Therefore, compared with current solutions, the proposed BCM exhibits the advantages of integration and miniaturization as well as the precise and flexible manipulations of the behaviors of EM and acoustic waves and may have potential applications in many scenarios. Furthermore, the proposed BCM may have potential applications in biphysical sensors, safety detection, and biphysical integrated communication.

ACKNOWLEDGMENTS

This work was supported by the National Natural Science Foundation of China (Grants No. 52305099 and No. 52305249) and Guizhou Provincial Basic Research Program (Natural Science) (Grant No. ZK (2022) 035).

DATA AVAILABILITY

The data that support the findings of this article are not publicly available. The data are available from the authors upon reasonable request.

[1] H. L. Wang, H. F. Ma, M. Chen, S. Sun, and T. J. Cui, A reconfigurable multifunctional metasurface for full-space control of electromagnetic waves, Adv. Funct. Mater. **31**, 2100275 (2021).

[2] S. W. Fan, S. D. Zhao, A. L. Chen, Y. F. Wang, B. Assouar, and Y. S. Wang, Tunable broadband reflective acoustic metasurface, Phys. Rev. Appl. **11**, 044038 (2019).

[3] L. Carpentier, A. Gueddida, G. Lévêque, R. Alcorta-Galvan, C. Croënne, M. Miniaci, B. Djafari-Rouhan, and Y. Pennec, Elliptic pillars based metasurface for elastic waves focusing in a plate, APL Mater. **12**, 041102 (2024).

[4] B. Liu, B. Ren, J. Zhao, X. Xu, Y. Feng, W. Zhao, and Y. Jiang, Experimental realization of all-angle negative refraction in acoustic gradient metasurface, Appl. Phys. Lett. **111**, 221602 (2017).

[5] B. M. Yao, Y. S. Gui, X. S. Chen, W. Lu, and C.-M. Hu, Experimental realization of negative refraction using one metasurface, Appl. Phys. Lett. **106**, 121903 (2015).

[6] F. Lin, W. Huang, X. He, and C. Li, Anomalous reflection beam steering based on high-bit coding metasurfaces, J. Optoelectron. Adv. Mater. **25**, 105 (2023).

[7] P. Zhang and Y. Dong, Broadband cross circularly polarized carpet invisibility cloak based on Pancharatnam–Berry phase reflective metasurface, Laser Phys. Lett. **20**, 076201 (2023).

[8] H. Lee and D. H. Kwon, Dual-polarized printed cylindrical metasurface cloak at microwave frequencies, Phys. Rev. Appl. **21**, 054031 (2024).

[9] T. J. Cui, Microwave metamaterials, Natl. Sci. Rev. **5**, 134 (2018).

[10] J. Sun and J. Zhou, Metamaterials: The art in materials science, Engineering **44**, 145 (2024).

[11] Y. Yang, H. Wang, F. Yu, Z. Xu, and H. Chen, A metasurface carpet cloak for electromagnetic, acoustic and water waves, Sci. Rep. **6**, 20219 (2016).

[12] C. Zhang, G. Y. Song, H. F. Ma, J. Yang, W. K. Cao, X. Y. Xie, P. Chen, Q. Cheng, L. T. Wu, and T. J. Cui, A metamaterial route to realize acoustic insulation and anisotropic electromagnetic manipulation simultaneously, Adv. Mater. Technol. **3**, 1800161 (2018).

[13] G. Song, C. Zhang, Q. Cheng, Y. Jing, C. Qiu, and T. Cui, Transparent coupled membrane metamaterials with simultaneous microwave absorption and sound reduction, Opt. Express **26**, 22916 (2018).

[14] G. D. Bai, Q. Ma, W. K. Cao, R. Q. Li, H. B. Jing, J. Mu, L. Bao, R. Y. Wu, C. Zhang, X. Wan, Q. Cheng, and T. J. Cui, Manipulation of electromagnetic and acoustic wave behaviors via shared digital coding metallic metasurfaces, Adv. Intell. Syst. **1**, 1900038 (2019).

[15] H. Sun, P. Hu, J. Wang, J. Zhao, R. Zhu, C. Ding, J. Zhang, Z. Liu, Z. Chu, Y. Cui, F. Wu, S. Qu, and J. Wang, Multi-physics metasurface with reduced characteristic scales simultaneously for microwave, infrared, and acoustic compatibility, Photon. Res. **13**, 263 (2025).

[16] Y. Zhou, J. Chen, R. Chen, W. Chen, Z. Fan, and Y. Ma, Ultrathin electromagnetic–acoustic amphibious stealth coats, Adv. Opt. Mater. **8**, 2000200 (2020).

[17] C. Zhang, W. K. Cao, J. Yang, J. C. Ke, M. Z. Chen, L. T. Wu, Q. Cheng, and T. J. Cui, Multiphysical digital coding metamaterials for independent control of broadband electromagnetic and acoustic waves with a large variety of functions, ACS Appl. Mater. Interfaces **11**, 17050 (2019).

[18] A. Díaz-Rubio and S. Tretyakov, Dual-physics metasurfaces for simultaneous manipulations of acoustic and electromagnetic waves, Phys. Rev. Appl. **14**, 014076 (2020).

[19] F. Sun, Y. Liu, and S. He, Surface transformation multi-physics for controlling electromagnetic and acoustic waves simultaneously, Opt. Express **28**, 94 (2020).

[20] Y. Zhou, J. Chen, L. Liu, Z. Fan, and Y. Ma, Magnetic–acoustic biphysical invisible coats for underwater objects, NPG Asia Mater. **12**, 27 (2020).

[21] J. Zhan, Y. Mei, K. Li, Y. Zhou, J. Chen, and Y. Ma, Conformal metamaterial coats for underwater magnetic-acoustic bi-invisibility, Appl. Phys. Lett. **120**, 094104 (2022).

[22] C. Cai, Y. Li, M. Li, Y. Qin, and Y. Zhou, Phase and amplitude simultaneously coding metasurface with multi-frequency and multifunctional electromagnetic modulations, Sci. Rep. **14**, 20904 (2024).

[23] L. W. Wu, H. F. Ma, Y. Gou, R. Y. Wu, Z. X. Wang, Q. Xiao, and T. J. Cui, Multitask bidirectional digital coding metasurface for independent controls of multiband and full-space electromagnetic waves, Nanophotonics **11**, 2977 (2022).

[24] S. Peng, A. Song, Y. Bai, C. Sun, and Y. Xiang, Reconfigurable frequency-selective acoustic coding metasurface for multifunctional wavefront manipulation, Appl. Acoust. **235**, 110658 (2025).

[25] A. Song, Y. Bai, C. Sun, Y. Xiang, and F. Z. Xuan, A reconfigurable acoustic coding metasurface for tunable and broadband sound focusing, J. Appl. Phys. **134**, 243104 (2023).

[26] Y. Hu, S. N. Chen, Y. Shi, X. Liu, and J. Y. Wang, Space-time coding metasurface for multifunctional holographic imaging, Adv. Mater. Technol. **9**, 2302164 (2024).

[27] B. Xie, K. Tang, H. Cheng, Z. Liu, S. Chen, and J. Tian, Coding acoustic metasurfaces, Adv. Mater. **29**, 1603507 (2017).

[28] T. J. Cui, M. Q. Qi, X. Wan, J. Zhao, and Q. Cheng, Coding metamaterials, digital metamaterials and programmable metamaterials, Light Sci. Appl. **3**, e218 (2014).

[29] Y. Ruan, J. Zhu, Q. Lin, Y. Wang, D. Zhou, S. Wang, C. Li, J. Shi, and R. Chen, Reflective vortex focusing for acoustic contact-free object rotation, J. Sound Vib. **581**, 118380 (2024).

[30] A. V. Sidorov, A. P. Veselov, and A. V. Vodopyanov, Dual-stream gas targets for a point source of vacuum and extreme ultraviolet radiation supported by focused electromagnetic radiation, Phys. Fluids **37**, 017141 (2025).

[31] X. Lin, W. Gu, J. Liu, and F. Zhang, A near-infrared optical metasurfaces aggregate used for nondestructive testing of transparent targets, Opt. Laser Technol. **186**, 112734 (2025).

[32] Y. Luo, M. L. Tseng, S. Vyas, H. Y. Kuo, C. H. Chu, M. K. Chen, H. C. Lee, W. P. Chen, V. C. Su, X. Shi, H. Misawa, D. P. Tsai, and P. C. Yang, Metasurface-based abrupt autofocusing beam for biomedical applications, Small Methods **6**, 2101228 (2022).

[33] S. Qi and B. Assouar, Ultrathin acoustic metasurfaces for reflective wave focusing, J. Appl. Phys. **123**, 234501 (2018).

[34] Q. Mai, C. Wang, X. Wang, S. Cheng, M. Cheng, Y. He, J. Xiao, H. Ye, D. Fan, Y. Li, and S. Chen, Metasurface based optical orbital angular momentum multiplexing for 100 GHz radio over fiber communication, J. Lightwave Technol. **39**, 6159 (2021).

[35] Y. Zhang, J. Gao, and X. Yang, Spatial variation of vector vortex beams with plasmonic metasurfaces, Sci. Rep. **9**, 9969 (2019).